



Article

Improved Coil Design for Magnetic Pulse Welding of Metallic Sheets

Rishabh Shotri ¹, Koen Faes ^{2,*}, Guillaume Racineux ³ and Amitava De ¹

¹ Mechanical Engineering Department, Indian Institute of Technology Bombay, Mumbai 400076, India
² Belgium Welding Institute, Technologiepark Zwijnaarde 48, 9052 Zwijnaarde, Belgium
³ Central School of Nantes, Research Institute in Civil and Mechanical Engineering, 44321 Nantes, France
* Correspondence: koen.faes@bil-ibs.be

Abstract: Magnetic pulse welding of overlapping dissimilar metallic sheets is an emerging technique and usually employs flat electromagnetic coils with rectangular-, H-, I-, and E-shaped cross-sections. The asymmetric cross-section of these coils results in a non-uniform electromagnetic field and in a non-uniform connection in the interface between the overlapping sheets. In this article, the use of a novel O-shaped flat coil is proposed to join an aluminium flyer sheet with a target steel sheet. A finite element-based numerical model is developed to calculate the electromagnetic field, flyer velocity, and its gradual impact onto the target, and the deformations of the sheet assembly. The calculated results with the O-shaped coil show a high-intensity electromagnetic field, the concentration of which decreases radially outwards in a uniform manner. The numerically computed and experimentally measured flyer velocity are found to be in fair agreement. The calculated results show a regularly decreasing impact behaviour between the flyer and target and their resulting deformation. The measured results show the formation of an annular ring-shaped joint profile that is generally found to be stronger compared to that obtained with flat coils with a rectangular cross-section.

Keywords: magnetic pulse welding; O-shaped flat coil; electromagnetic field; impact and deformation analysis; numerical modelling; experimental investigations



Citation: Shotri, R.; Faes, K.; Racineux, G.; De, A. Improved Coil Design for Magnetic Pulse Welding of Metallic Sheets. *J. Manuf. Mater. Process.* **2022**, *6*, 144. <https://doi.org/10.3390/jmmp6060144>

Academic Editor: Paul Kah

Received: 7 October 2022

Accepted: 14 November 2022

Published: 16 November 2022

Publisher's Note: MDPI stays neutral with regard to jurisdictional claims in published maps and institutional affiliations.



Copyright: © 2022 by the authors. Licensee MDPI, Basel, Switzerland. This article is an open access article distributed under the terms and conditions of the Creative Commons Attribution (CC BY) license (<https://creativecommons.org/licenses/by/4.0/>).

1. Introduction

Magnetic pulse welding (MPW) uses high-frequency, intense electrical energy to produce a transient electromagnetic (EM) field and pressure that cause a rapid impact and solid-state coalescence along the interface between overlapping metallic sheets [1–4]. A typical MPW arrangement is shown in Figure 1a with the coil and overlapping sheets, which are referred to as flyer (top) and target (bottom). The flyer or a segment of it is directed by the EM pressure and collides with it with a high speed in a progressive manner, resulting in mechanical deformation and joining between the sheets, as illustrated in Figure 1b. The coalescence between the sheets occurs in solid state and within only a few tens of micro-seconds [5]. The EM coil provides the required EM pressure concentration onto the flyer and thus, finding an appropriate coil design is critical for MPW of metallic sheets [1,2,5]. The published literature shows that a systematic evaluation of diverse coil cross-sections for improving the joint profile for MPW of sheets has started only recently [6]. The present work also focuses on a systematic attempt to evaluate an improved coil design for MPW of metal sheets.

The EM field and pressure distributions in MPW notably depend on the coil cross-section [7,8]. Detailed research is currently being performed on joining metal sheets using different coil designs [9–11]. Figure 2a–c show flat EM coils with rectangular-, H/I-, and E-shaped cross-sections, which are used for MPW of sheets [12–24]. The cross-sectional area of the rectangular coils (Figure 2a) was varied from 2.8×8 to 4×10 mm², with the corresponding applied energy from 10 to 40 kJ [12–14]. The rectangular coils could produce a maximum EM field of around 21 T and a pressure of around 176 MPa for joining of

sheets [12–14]. Coils with a trapezoid cross-section were used with the applied energy ranging from 2 to 10 kJ, which yielded a maximum EM field from 14 to 16 T, and a pressure from 78 to 102 MPa [15–18]. The cross-sections of the H/I- (Figure 2b) and the E-shaped (Figure 2c) coils decrease inward and result in an increasing EM field towards the mid-segment of the coil–flyer overlapping region [19–23]. The effective area of the cross-section of H/I-shaped coils was varied from 5×5 to 8×10 mm² for an applied energy from 2.0 to 13.7 kJ [17–21]. The average area of the cross-section of the E-shaped coils was varied from 5×8 to 10×15 mm² for an applied energy from 6.3 to 13.5 kJ [24,25]. The H/I/E-shaped coils could generate a maximum EM field of around 27 to 36 T and a resulting pressure of around 290 to 516 MPa [23,24].

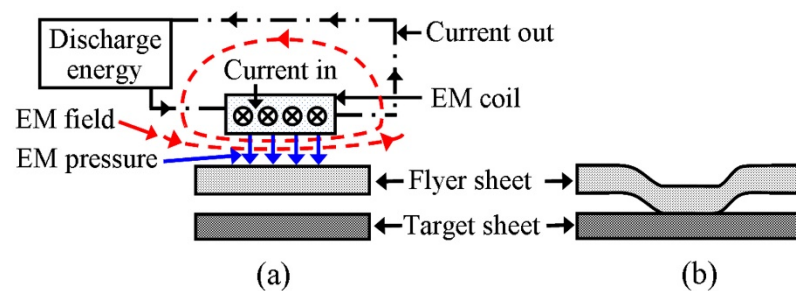


Figure 1. Schematic views of (a) MPW arrangement with coil and overlapping sheets, and (b) joint configuration.

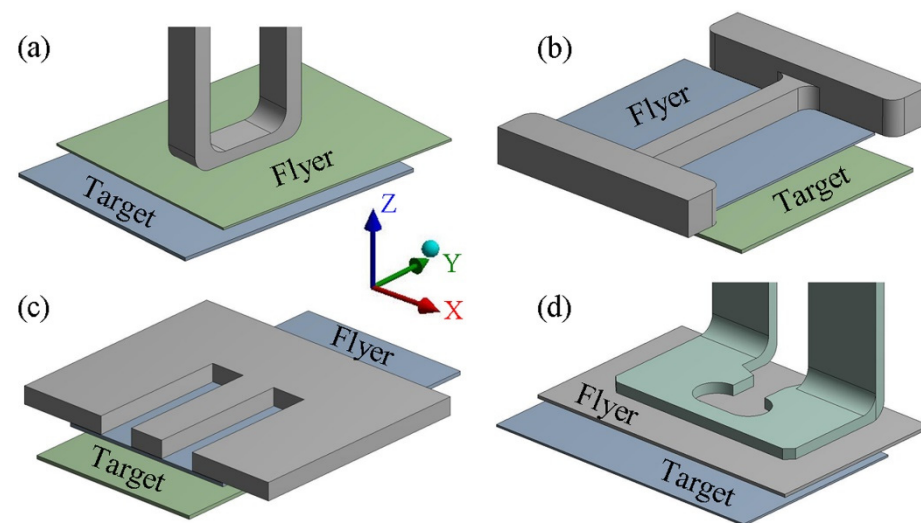


Figure 2. Flat EM coils with (a) rectangular-shaped, (b) H/I-shaped, (c) E-shaped, and (d) O-shaped cross-sections for MPW of sheets.

Although the H/I- and E-shaped coil cross-sections provided an inward concentrated EM field and pressure, these were generally non-uniform in nature due to the sharp change of the coil cross-sections. The resulting impact progression and plastic deformation between the overlapping sheets remained unsuitable to achieve a good coalescence [26]. In contrast, an O-shaped EM coil (Figure 2d) with a uniformly reducing radial cross-section appears to create a regular EM field with an inward concentration and resulting pressure [27]. Detailed investigations on MPW of overlapping sheets with O-shaped EM coils are therefore of significant interest.

A coupled experimental and theoretical investigation is presented here to examine the suitability of an O-shaped EM coil to weld aluminium and steel sheets using multiple combinations of the standoff distance between the overlapping sheets and the applied energy. The theoretical work includes the development of a numerical model for estimation of the time-varying EM field as well as the pressure. The resulting impact progression of

the flyer and the deformation of the overlapping sheets are computed using a dynamic mechanical analysis. The experimental investigation involves the measurement of the discharge current, the flyer velocity, and the dimensions of the welded interface and joint strength.

2. Experimental Set-Up

Figure 3a shows the charging and discharge circuits, and the original joint assembly with an O-shaped coil. The discharge circuit includes a capacitance (C) of $408 \mu\text{F}$, resistance (R) of $6 \text{ m}\Omega$, and inductance (L) of $0.141 \mu\text{H}$. The applied energy confirms a damped sinusoidal form with a high frequency ($f = 20.5 \text{ kHz}$) and damping rate ($\tau = 13,442 \text{ s}^{-1}$). The discharge circuit releases the current by a switch (S_g). The real-time current waveform is recorded using a Rogowski coil. The flyer velocity is monitored in real-time by a Photon Doppler Velocimeter (PDV) with its collimator probe positioned to face the flyer through a central hole in a rigid block, which is used as a target for velocity measurement.

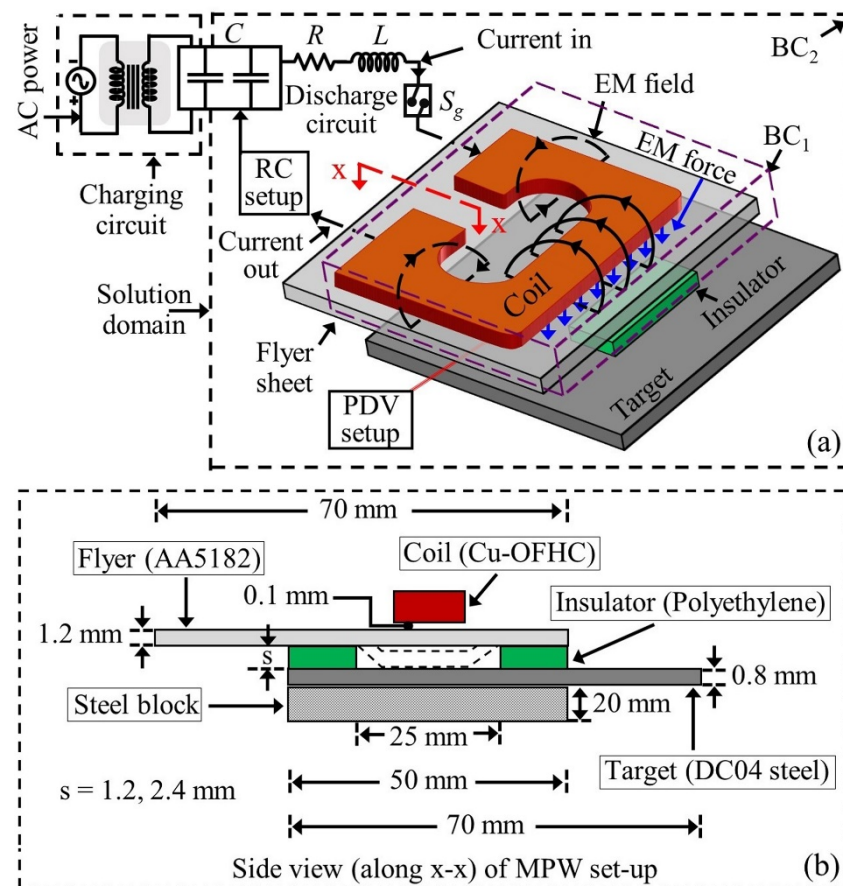


Figure 3. (a) MPW set-up with an O-shaped coil, and (b) a side view of the original joint assembly with the coil along the x-x section, shown in (a).

Figure 3b shows a side view of the original joint assembly with the coil along a section x-x, as indicated in Figure 3a. The overlapping sheets are located underneath the coil and are separated at different standoff distances using two adjacent insulator blocks with different thicknesses (Figure 3b). The distance between the insulators guides the impact and the plastic deformation. The sheets were placed on a thick steel block, which resists the downward movement of the assembly. The sheet and insulator materials and their dimensions are shown in Figure 3b. Tables 1 and 2 shows the sheet material compositions, which were obtained from the manufacturer’s material certificate and equivalently cited based on [26,27]. The overlapping area of the cross-section between the sheets equals

$50 \times 110 \text{ mm}^2$. The coil cross-section area varies from 4×8 to $4 \times 30 \text{ mm}^2$. The welds were made at three different applied energy values of 10, 13, and 16 kJ, and two values of the standoff distance(s), as shown in Figure 3b. The joint strength of the welded specimens was measured by lap shear testing. The quasi-static lap shear tests were performed using an INSTRON 5584 machine (150 kN capacity) at a displacement rate of 0.01 mm/s. The welded specimens were subjected to dynamic lap shear testing, using an MTS machine (20 kN) at a displacement rate of 614 mm/s. The contact zone profile was measured using an optical microscope after peeling off the flyer and polishing the exposed interface.

Table 1. Chemical composition (max. %at.) of AA5182 (flyer) [27].

Flyer	Si	Fe	Cu	Mn	Mg	Cr	Zn	Ti	Al
AA5182	0.20	0.35	0.15	0.50	4.0–5.0	0.10	0.25	0.10	balance

Table 2. Chemical composition (max. %at.) of DC04 steel (target) [26,27].

Target	C	Mn	Si	P	S	Al	Fe
DC04	0.08	0.40	0.10	0.025	0.025	0.020	balance

3. Theoretical Investigations

The EM field (\mathbf{H}) inside the EM domain (Figure 3) was computed using Maxwell's (diffusion) governing equation [28,29]:

$$\frac{1}{\mu\sigma} \nabla^2 \mathbf{H} = \frac{\partial \mathbf{H}}{\partial t} \quad (1)$$

where, t is the time variable, μ is the magnetic permeability, and σ is the electrical conductivity of the conductors. Figure 3a shows a near-field boundary BC_1 and a far-field boundary BC_2 . The EM field is assumed continuous along BC_1 and negligible along BC_2 . Other boundary condition details are available in [28–31] and are not repeated here. The EM pressure (p) on the flyer is calculated as [14]:

$$p = \frac{1}{2} \mu_0 \mu_r (H_s^2 - H_p^2) \quad (2)$$

where H_s and H_p are the computed EM fields, respectively, on the top surface (facing the coil) and the bottom surface (facing the target) of the flyer, μ_0 is the air permeability, and μ_r is the flyer permeability. The EM analysis computes the distribution of the current density and the EM field in the coil–sheet assembly. The EM pressure was calculated from the computed EM field intensity using Equation (2). The dynamic mechanical analysis used the time-varying EM pressure (p) as input to calculate the velocity and acceleration of the flyer [32]. The deformation of the sheets was assumed to have a viscoplastic behaviour, which was modelled using a Johnson–Cook constitutive relation [33]. Further details of the numerical model are provided in Appendix A.

4. Results

4.1. Computed Results from the EM Model

Figure 4a,b present the calculated EM field (Figure 4a) and pressure (Figure 4b) for an O-type coil for an applied energy of 13 kJ and at a time instant of 11 μs . A fairly uniform concentration of the EM field towards the centre of the coil–flyer overlapping region was obtained, due to the radially inward decreasing cross-section of the O-shaped coil (Figure 4a). The computed EM pressure also showed an inward concentrating pattern similar to that of the EM field (Figure 4b). The maximum obtained EM field was around 32 T and the estimated maximum pressure was around 432 MPa. As the applied energy was varied from 10 to 16 kJ, the maximum EM field using the O-shaped coil increased from

27 to 39 T. The maximum EM pressure also increased from 290 to 605 MPa. For the same applied energy with a flat rectangular-shaped coil, the maximum EM field and pressure were computed as 19 T and 157 MPa [30], respectively, which are significantly smaller than those obtained with the O-type coil. Figure 4c,d show the computed EM pressure with a H/I-shaped coil and an E-shaped coil, respectively, for an applied energy of 13 kJ and at a time instant of 11 μ s. All other parameters were considered equal. Figure 4c shows that the calculated EM pressure distribution was concentrated along the active segment of an H/I-shaped flat coil with a peak value of 253 MPa. Likewise, Figure 4d shows the computed EM pressure distribution along the active segment of an E-shaped flat coil with a peak value equal to 316 MPa. A comparison of Figure 4b–d clearly shows that the O-type coil yielded a much higher EM pressure concentration along its active segment compared to the other coil geometries.

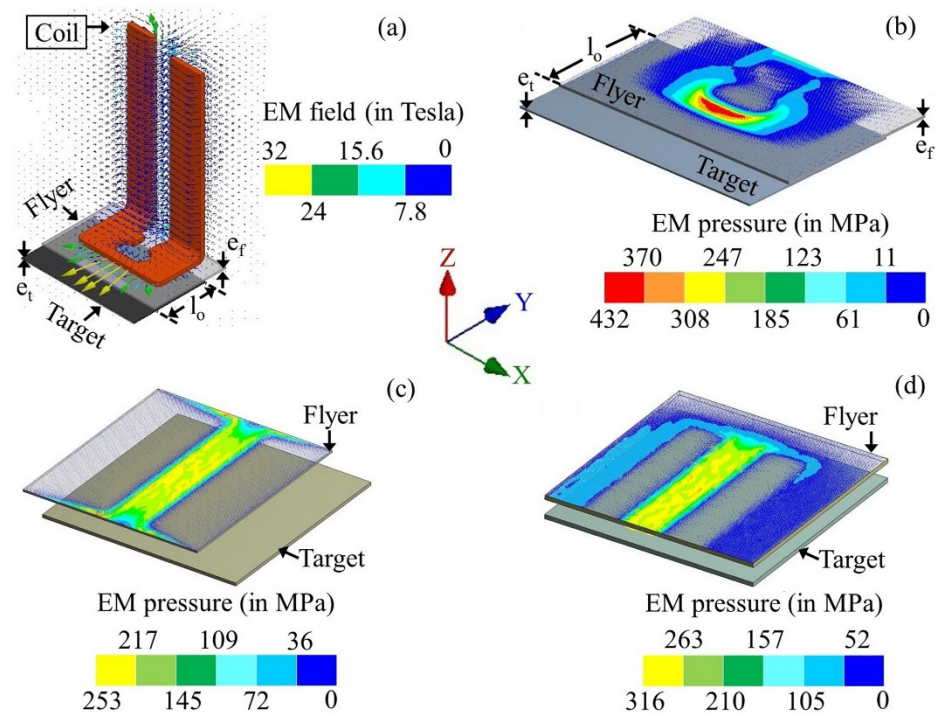


Figure 4. Calculated (a) EM field intensity and (b) EM pressure distribution with an O-shaped flat coil, and EM pressure distribution with a (c) H/I-shaped flat coil and (d) E-shaped flat coil for an applied energy of 13 kJ and at a time instant of 11 μ s for MPW of a 1.2 mm (e_f) flyer and 0.8 mm (e_t) target.

Figure 5 shows the calculated pressure distribution on an AA5182 flyer for a rectangular- (Figure 5a) and an O-shaped (Figure 5b) EM coil for an applied energy of 10 kJ. A comparison of Figure 5a,b depicts the pressure variation in the central region from 105 to 157 MPa, and from 274 to 366 MPa, respectively, for the rectangular- and O-shaped coils, which reveals the effectiveness of the O-shaped coil to augment the EM pressure concentration. When the applied energy was increased further to 13 and 16 kJ using the O-shaped coil, the EM pressure concentration in the central region showed a remarkable increase (Figure 5c,d).

4.2. Computed Results from Mechanical Analysis

Figure 6a presents the calculated pressure and the computed and measured flyer velocity for the duration of the applied energy with an O-shaped coil. The flyer velocity increased steeply to a peak value and closely followed the nature of the applied pressure. The subsequent sharp decrease of the flyer velocity indicated its impact on the target, after which the flyer stopped moving. The peak computed EM pressure was around 235 to 340 MPa for an applied energy of 10 to 16 kJ. An analytical estimation of the EM pressure

using similar process conditions is shown in Appendix B, which also provided a similar range of values. The computed values of the EM pressure with an O-shaped coil are therefore considered correct.

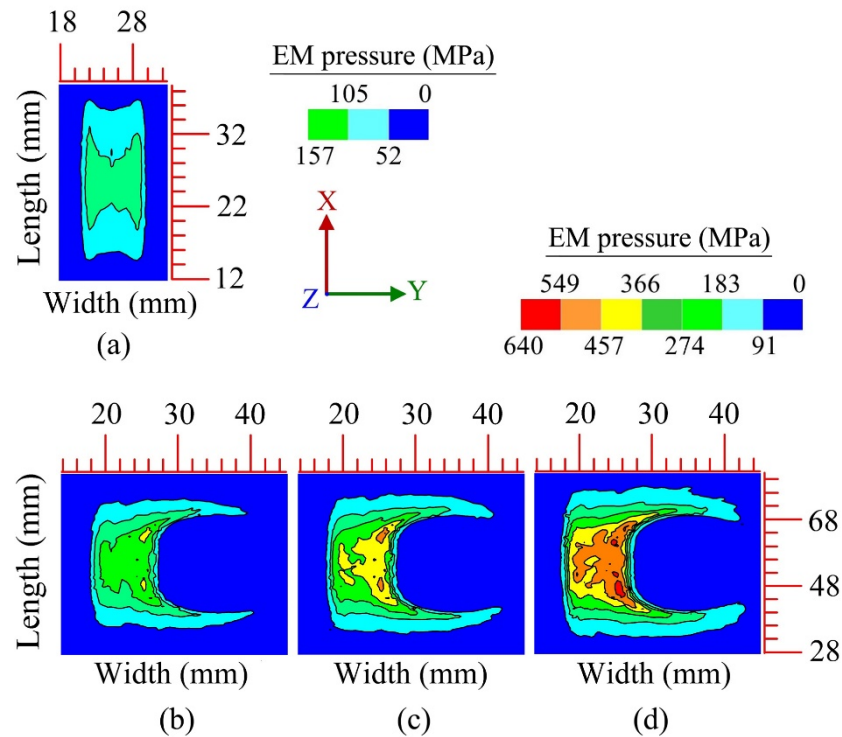


Figure 5. Computed EM pressure distribution on AA5182 aluminium alloy flyer with (a) rectangular- and (b–d) O-shaped flat coils for applied energy of (a,b) 10, (c) 13, and (d) 16 kJ.

Figure 6b shows the calculated and measured impact velocity of the flyer for different settings of the standoff distance and the applied energy, using an O-shaped coil. The calculated impact velocity showed slight over-estimation compared to the corresponding measured values, which is due to the relatively simplified coupling between the EM and mechanical analysis. The impact velocity increased with the standoff distance and the applied energy. A higher impact velocity for a greater standoff distance occurred as the flyer moved and accelerated over a larger distance. Likewise, a greater applied energy resulted in higher impact velocity because of the stronger EM field and pressure. The measured velocity at impact varied from 3.0×10^5 to around 4.4×10^5 mm/s, which are slightly higher compared to the values obtained with a flat rectangular EM coil for similar conditions [32]. An analytical estimation of the impact velocity also showed a similar order of magnitude, as illustrated in Appendix B.

Figure 7 shows the computed flyer–target plastic deformation with progress in time for an O-shaped coil. Figure 7a shows the entire flyer–target assembly. The calculated deformation is highlighted for the region enclosed within the red dashed rectangle in Figure 7a for clarity. The onset of the flyer–target deformation behaviour is presented in Figure 7b,c. The peak EM pressure and plastic deformation shown in Figure 7b,c were 175 MPa and 1.43 mm, and 228 MPa and 2.61 mm, respectively. The flyer deformation increased to approximately 2.67 mm (Figure 7d,e) with the increase in time. The corresponding computed peak EM pressures were 98 and 1.3 MPa, respectively. The decrease of the EM pressure was caused by the progression of the impact and the displacement of the flyer away from the coil, which reduced the intensity of the EM field on the flyer.

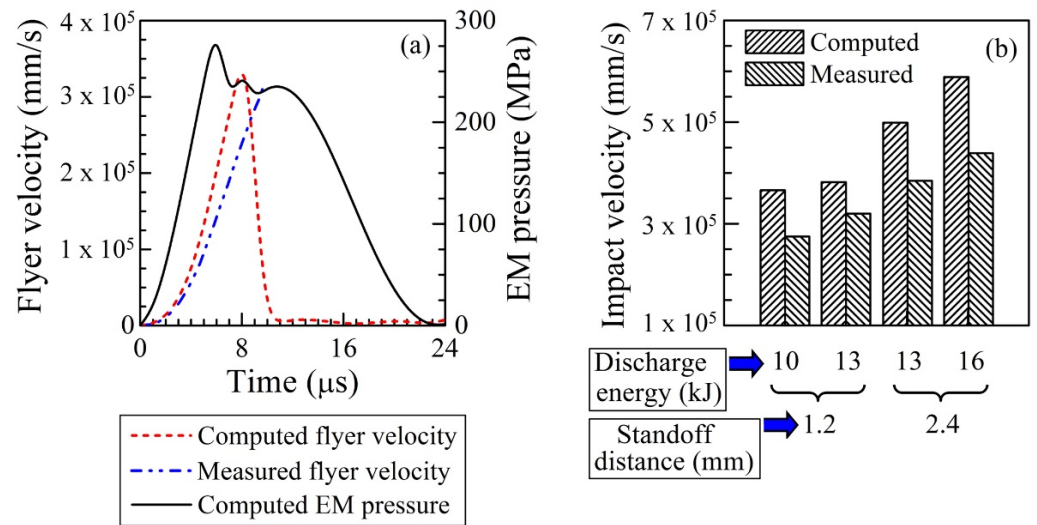


Figure 6. (a) Computed EM pressure and computed and measured flyer velocity for a duration of 24 μs. Process conditions: O-shaped coil, applied energy = 13 kJ, standoff distance = 1.2 mm. (b) Impact velocity of flyer for multiple standoff distance and applied energy combinations.

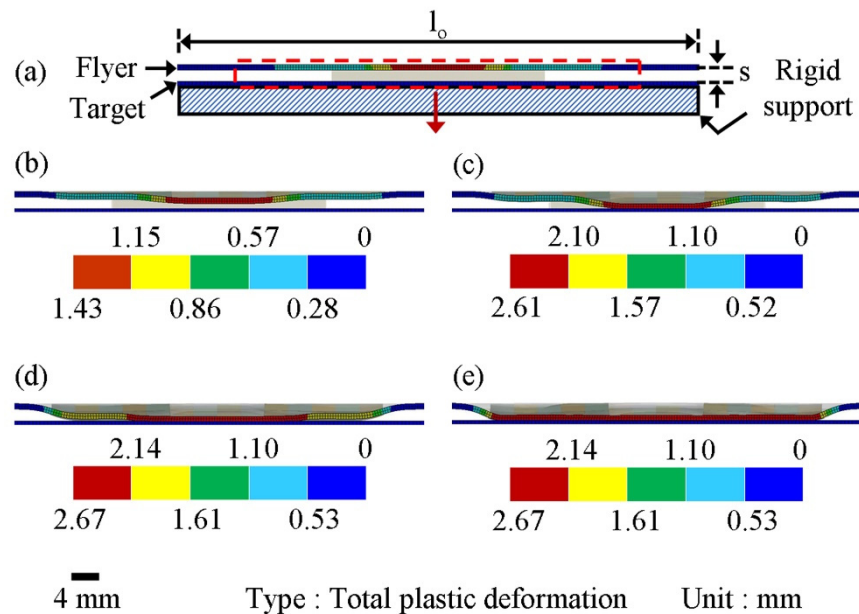


Figure 7. (a) Computed plastic deformation of flyer (AA5182)–target (DC04 steel) assembly with an O-shaped flat coil at successive times of (a) 4, (b) 9.6, (c) 12, (d) 16.8, and (e) 24 μs. Process conditions: applied energy = 13 kJ, standoff distance = 2.4 mm.

Figure 8 presents the computed impact angle and velocity of the flyer and the flyer–target collision velocity as a function of time using an O-shaped coil. Figure 8a shows that the impact angle increased with time, which occurred as the flyer continued to impact the target and the remaining portion of the flyer bent away from the target. The impact angle was strongly influenced by the standoff distance and relatively little by the applied energy. Corresponding to an applied energy and standoff distance of 13 kJ and 1.2 mm, the maximum impact angle was 3.4°. When the standoff distance increased to 2.4 mm, the maximum impact angle became 6.5°. In contrast, the maximum flyer impact angle showed little change when the applied energy varied from 13 to 16 kJ. Figure 8b shows a similar effect of the applied energy and standoff distance on the impact velocity. Corresponding to an applied energy and standoff distance of 13 kJ and 1.2 mm, the maximum impact velocity

was 3.25×10^5 mm/s. As the standoff distance increased to 2.4 mm, the maximum impact velocity became 5.23×10^5 mm/s. An increase of the applied energy from 13 to 16 kJ has resulted in a very small increase of the impact velocity.

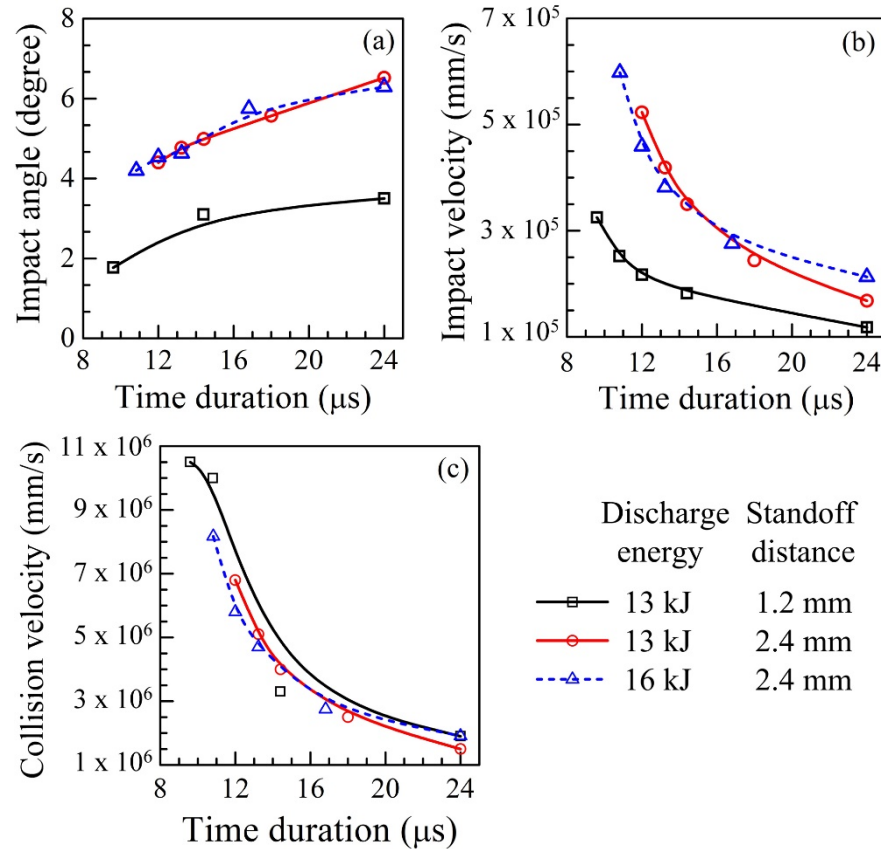


Figure 8. Computed impact (a) angle and (b) velocity of the flyer, and (c) flyer–target collision velocity variation with time, for different values of the standoff distance and applied discharge energy.

Figure 8c shows the progress of the collision velocity, which was calculated as the ratio of the impact velocity and the sine of the impact angle [34–36]. As the flyer impact progressed, the impact angle increased, and the impact velocity was reduced, which resulted in a smaller collision velocity. A good interface coalescence was obtained when the collision velocity and the stress wave velocity in the flyer and target materials were in the same order of magnitude [34–37]. The stress wave velocity in materials was computed as $(E/\rho)^{0.5}$, where ρ is the density and E is the modulus of elasticity. The stress wave velocity in the flyer (AA5182) was around 5.10×10^6 mm/s and in the target (steel), it was around 4.78×10^6 mm/s. These values are similar to the collision velocities obtained in between the time instants of 11 to 14 μ s, approximately, for different process conditions.

4.3. Weld Characteristics

Figure 9 shows a ring-shaped annular elliptical weld profile obtained during MPW with a rectangular- (Figure 9a) and an O-shaped coil (Figure 9b). The dimensions g_{lo} , g_{to} , g_{li} , and g_{ti} , as shown in Figure 9, were measured using an optical microscope, and the area of the weld cross-section was calculated as $\pi(g_{lo}g_{to}-g_{li}g_{ti})$ [32]. The maximum and minimum widths of the ring-shaped annular welds were considered by comparing the differences between g_{lo} and g_{li} , and g_{to} and g_{ti} . A comparison of Figure 9a,b shows that the weld profile was nearly symmetric when using the rectangular coil, but slightly asymmetric against the longitudinal axis for the O-shaped coil. This is attributed to the radially inward EM pressure concentration obtained with an O-shaped coil, as shown in the Figure 5b–d,

that slightly offset the central transverse impact between the sheets. As a result, the weld cross-section assumed a slight inward bulge, as shown schematically in Figure 9b.

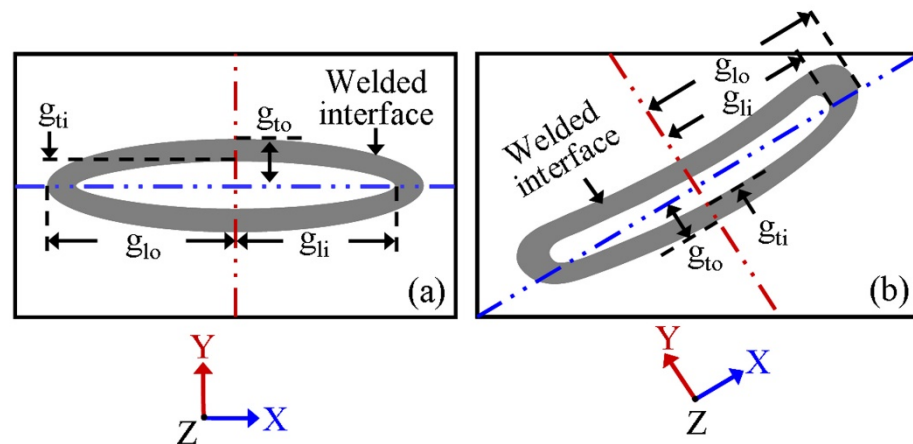


Figure 9. Schematic representation of the weld interface over the target for MPW of sheets using (a) rectangular- and (b) O-shaped flat coils.

Figure 10 shows the ring-shaped annular elliptical welds in grey for an O-shaped coil and for four different conditions. The welds were longitudinally aligned with a slight inward bulge. A comparison of Figure 10a–d shows that the area of the cross-section and width of the welds increased with both the standoff distance and the applied discharge energy, which is intuitive. The measured value of the area of the cross-section of the annular elliptical weld was 60 mm^2 for an applied energy of 10 kJ and a standoff distance of 1.2 mm (Figure 10a). With an increase in the applied energy to 13 kJ, the cross-sectional area of the annular elliptical weld increased to 76 mm^2 (Figure 10b). The maximum cross-sectional area of the annular elliptical weld was obtained as 95 mm^2 for the highest values of the applied energy of 16 kJ and the standoff distance of 2.4 mm (Figure 10d). The maximum widths of the annular welds in the longitudinal direction were found to be around 2.1 (Figure 10a) and 3.75 mm (Figure 10d). In contrast, the minimum widths of the annular welds in the transverse direction were found to be around 1.35 (Figure 10a) and 1.9 mm (Figure 10d).

Figure 11a,b show a welded joint of AA5182 and DC04 steel sheets for an applied energy of 13 kJ and a standoff distance of 2.4 mm before and after lap shear testing. The lap shear tests were carried out in the quasi-static condition using a cross-head speed of 0.01 mm/s. Three samples were tested for each welding condition. It can be noted in Figure 11a that the outer boundary of the elliptical weld profile exhibited a slightly inward bend, as mentioned earlier for Figures 9b and 10. Figure 11b shows the tearing of the AA5182 sheet near the welded joint. The maximum loads at failure for the welds were found to be in the range of 6.1 to 6.5 kN for the conditions considered here [26,27]. The dynamic lap shear tests of the welded specimens obtained for a higher cross-head speed of around 0.6 m/s have shown that the maximum loads at failure were in the range of 7.5 to 8.2 kN for the conditions considered here [26,27]. For a similar range of process conditions, the welds between aluminium and steel sheets made with a rectangular coil can provide a maximum load of only about 2.5 kN [32].

In summary, a detailed investigation of MPW with an O-shaped coil was reported here to improve the joint formation between sheets. The influence of important process conditions on the EM field and pressure, the flyer impact phenomena, and deformation of flyer–target assembly, and the annular weld joint profile were illustrated. Further efforts are in progress for the improvement of the O-shaped coil design to achieve a straight hollow elliptical weld interface and for joining of sheets with relatively larger thicknesses.

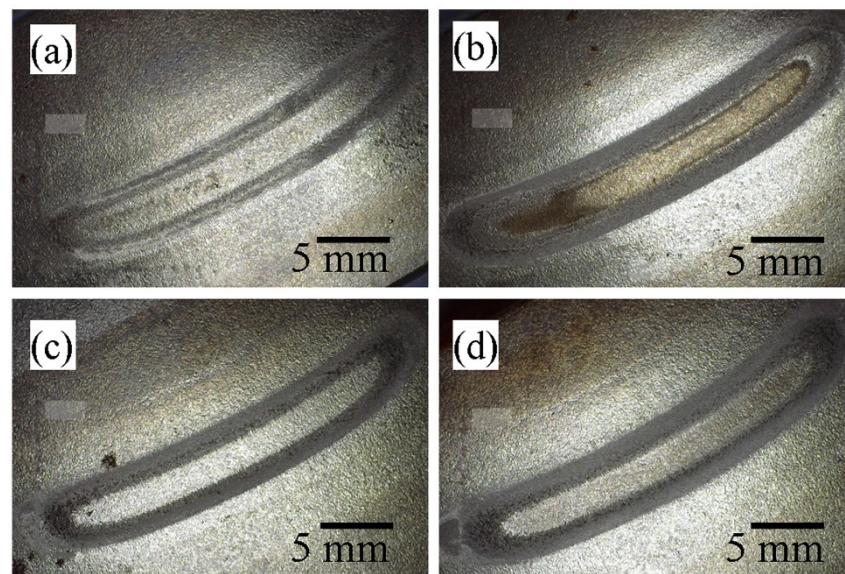


Figure 10. Ring-shaped annular elliptical weld profiles obtained with an O-shaped flat coil. Annular grey region indicates the fracture surface after complete separation of the flyer and target sheets during peel testing. Process conditions: applied energy (a) 10, (b,c) 13, and (d) 16 kJ, standoff distance (a,b) 1.2 and (c,d) 2.4 mm, and flyer sheet—AA5182, target sheet—DC04 steel.

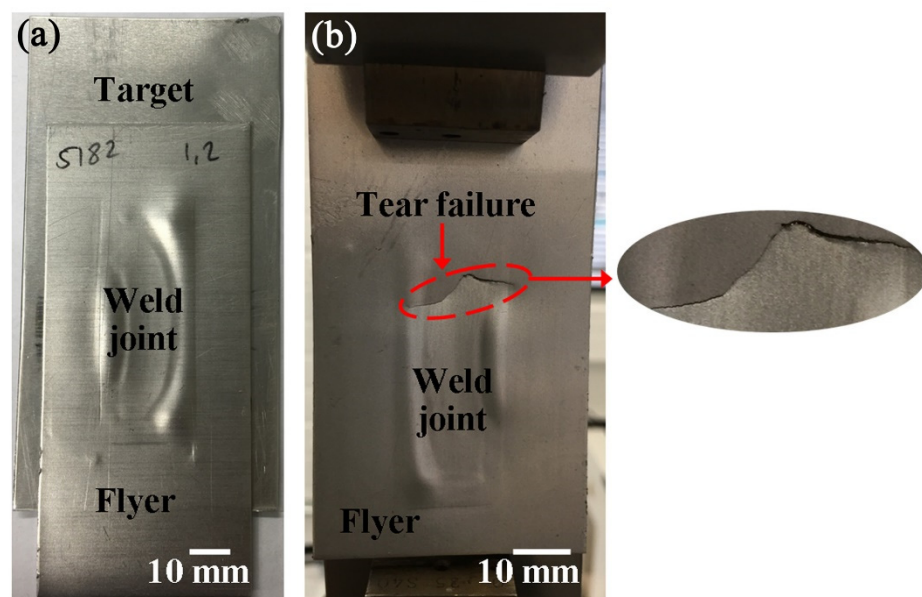


Figure 11. Welded sample obtained with an O-shaped coil (a) before and (b) after lap shear testing. The fracture near the periphery of the weld, which emerged during lap shear testing, is shown in detail for better clarity. The AA5182 sheet is cracked near the weld. Process conditions: applied discharge energy—13 kJ, standoff distance—2.4 mm, flyer sheet—AA5182, target sheet—DC04 steel.

5. Conclusions

The following are the main conclusions of the present work:

- Good welds between AA5182 flyer sheets and steel target sheets were produced for a range of standoff distances (1.2 and 2.4 mm) and applied energies (10, 13, and 16 kJ) using an O-shaped flat coil.
- The computed results have shown that an O-shaped flat coil can produce a significantly larger EM field and pressure concentration than rectangular-, H/I-, and E-shaped flat coils. For example, the maximum EM pressure with an O-shaped coil was found to be

around 3.5 times higher in comparison to that obtained using a flat rectangular coil for similar process conditions

- The EM field and pressure were also more regular for the O-shaped coil than for the other coils. The EM field and pressure concentrated radially inward as the cross-sectional area of the O-shaped coil decreased.
- The welded interface produced with the O-shaped coil showed a nearly annular elliptical geometry due to the inward EM pressure concentration. Both the standoff distance and the discharge energy directly influenced the final joint cross-sectional area.
- For similar process conditions, the O-shaped coil could produce an almost 3 times stronger joint between aluminium and steel sheets, compared to the joint obtained using a rectangular-shaped coil.

Author Contributions: Conceptualization, G.R. and R.S.; methodology, G.R., R.S. and A.D.; software, R.S. and A.D.; validation, G.R.; investigation, R.S. and G.R.; resources, G.R. and A.D.; writing—original draft preparation, R.S. and K.F.; writing—review and editing, R.S., K.F., G.R. and A.D.; visualization, R.S. and G.R.; supervision, A.D.; project administration, G.R. and A.D.; funding acquisition, K.F. All authors have read and agreed to the published version of the manuscript.

Funding: This research received no external funding.

Institutional Review Board Statement: Not applicable.

Informed Consent Statement: Not applicable.

Data Availability Statement: Not applicable.

Conflicts of Interest: The authors declare no conflict of interest.

Appendix A

Table A1 below provides the material properties used for the calculations.

Table A1. Flyer and target material properties [24,25,32].

Parameter	Specification	Unit	AA5182	DC04 Steel
μ	Relative permeability	-	1.0	B-H curve [32]
σ	Electrical conductivity	S/m	16.3×10^6	7.54×10^6
ρ, c_p	Density, specific heat	kg/m ³ , J/kg/K	2650, 902	7870, 470
E, G	Elastic modulus, shear modulus	GPa, GPa	69.6, 26	180, 69.2
T _m	Melting temperature	K	873	1788
Johnson–Cook material strength parameters				
A, B	Initial flow stress, hardening constant	MPa, MPa	109, 552	162, 598
C, n	Strain rate sensitivity, hardening exponent	-	0.0012, 0.4	2.623, 0.6
m	Thermal softening coefficient	-	3.19	0.009

The numerical model was contemplated using the finite element analysis software ANSYS (ver. 14.5, ANSYS Inc., Canonsburg, PA, USA) with around 248,000 to 272,000 solid tetrahedral elements for the EM analysis and around 52,500 to 60,000 solid hexahedral elements for the mechanical analysis [38]. The calculations were performed with a very small timestep (1×10^{-6} s) [32]. The EM analysis provided the EM pressure distribution on the flyer at the end of every timestep. The computed pressure distribution was prepared as a special input file for the mechanical analysis, using a specially written script in MATLAB (MathWorks Inc., Natick, MA, USA). The results of the mechanical analysis, i.e., the flyer impact velocity and the deformation of the sheet assembly, were examined at selected timesteps to examine their evolution throughout the energy application period.

Appendix B

The EM pressure (p) for joining of sheets was estimated analytically as [31]:

$$P = C_L \left(\frac{U \mu_r \epsilon_c f}{w_c^3 L \tau} \right) \tag{A1}$$

where μ_f is the magnetic permeability of the flyer (12.56×10^{-7} H/m), and C_L is a “concentration length factor” and is equal to l_{of}/l_{rc} (~ 0.2), with l_{of} and l_{rc} as the length of the active (front turn, i.e., 80 mm) and the non-active segments of the O-shaped coil (396 mm). The terms e_c and w_c are the thickness (4 mm) and width (8 mm) of the coil front turn. The flyer impact velocity (v_i) was estimated analytically as [31]:

$$v_i = \sqrt{\frac{P}{\rho_f}} \left(\frac{s}{e_f} \right) \quad (\text{A2})$$

where ρ_f is the material density (i.e., 2650 kg/m³) and e_f is the flyer thickness. Equations (A1) and (A2) can be used to analytically estimate p and v_i . For example, Equation (A1) provides $p = 340$ MPa when the applied energy is equal to 16 kJ. Correspondingly, Equation (A2) provides $v_i = 7.1 \times 10^5$ mm/s for $p = 340$ MPa and s (standoff distance) = 1.2 mm.

Appendix C

Table A2. Process conditions.

Parameter	Specification	Unit	Values
U	Applied energy	kJ	10, 13, 16
e_f, e_t	Flyer, target sheet thickness	mm	1.2, 0.8
s	Standoff distance	mm	1.2, 2.4

References

- Saadouki, B.; Sapanathan, T.; Pelca, P.H.; Elghorba, M.; Rachik, M. Fatigue damage in field shapers used during electromagnetic forming and welding processes at high frequency impulse current. *Int. J. Fatigue* **2018**, *109*, 93–102. [CrossRef]
- Mamalis, A.G.; Manolakos, D.E.; Kladas, A.G.; Koumoutsos, A.K. Electromagnetic Forming Tools and Processing Conditions: Numerical Simulation. *Mater. Manuf. Process.* **2006**, *21*, 411–423. [CrossRef]
- Zhang, S.; Lueg-Althoff, J.; Hahn, M.; Tekkaya, A.E.; Kinsey, B.L. Effect of Process Parameters on Wavy Interfacial Morphology During Magnetic Pulse Welding. *J. Manuf. Sci. Eng.* **2021**, *143*, 011010. [CrossRef]
- Zhang, W.; Xie, J.; Chen, Y.; Zhang, L.; Yin, L.; Zhang, T.; Wang, S. Interfacial microstructure and bonding mechanism of the Al/Ti joint by magnetic pulse welding. *Scr. Mater.* **2022**, *210*, 114434. [CrossRef]
- Zhou, Y.; Li, C.; Shi, X.; Wang, P.; Shen, T.; Mi, Y.; Ma, Y. Evaluation model of electromagnetic pulse welding effect based on Vc- β trajectory curve. *J. Mater. Res. Technol.* **2022**, *20*, 616–626. [CrossRef]
- Zhang, H.; Liu, N.; Li, X.; Wang, Q.; Ding, H. Optimization design and experimental research of magnetic pulse welding system based on uniform pressure electromagnetic actuator. *Int. J. Adv. Manuf. Technol.* **2022**, *121*, 8447–8465. [CrossRef]
- Yan, Z.; Xiao, A.; Cui, X.; Guo, Y.; Lin, Y.; Zhang, L.; Zhao, P. Magnetic pulse welding of aluminum to steel tubes using a field-shaper with multiple seams. *J. Manuf. Process.* **2021**, *65*, 214–227. [CrossRef]
- Soni, M.; Ahmed, M.; Panthi, S.K.; Kumar, S. Effect of coil design parameters on performance of electromagnetic forming process. *Mater. Manuf. Process.* **2022**, *37*, 64–80. [CrossRef]
- Yao, Y.; Jing, L.; Wang, S.; Li, G.; Cui, J.; Tang, X.; Jiang, H. Mechanical properties and joining mechanisms of Al-Fe magnetic pulse welding by spot form for automotive application. *J. Manuf. Process.* **2022**, *76*, 504–517. [CrossRef]
- Li, J.; Sapanathan, T.; Raoelison, R.; Hou, Y.; Simar, A.; Rachik, M. On the complete interface development of Al/Cu magnetic pulse welding via experimental characterizations and multiphysics numerical simulations. *J. Mater. Process. Technol.* **2021**, *296*, 117185. [CrossRef]
- Wang, P.; Ning, X.; Du, J.; Li, C. Electromagnetic pulse welding on a magnesium–aluminum joint: Role of angle of welding. *Mater. Manuf. Process.* **2022**, 1–8. [CrossRef]
- Zhu, C.; Sun, L.; Gao, W.; Li, G.; Cui, J. The effect of temperature on microstructure and mechanical properties of Al/Mg lap joints manufactured by magnetic pulse welding. *J. Mater. Res. Technol.* **2019**, *8*, 3270–3280. [CrossRef]
- Cui, J.; Ye, L.; Zhu, C.; Geng, H.; Li, G. Mechanical and Microstructure Investigations on Magnetic Pulse Welded Dissimilar AA3003-TC4 Joints. *J. Mater. Eng. Perform.* **2020**, *29*, 712–722. [CrossRef]
- Li, Y.; Yang, D.; Yang, W.; Wu, Z.; Liu, C. Multiphysics Numerical Simulation of the Transient Forming Mechanism of Magnetic Pulse Welding. *Metals* **2022**, *12*, 1149. [CrossRef]
- Kore, S.; Date, P.; Kulkarni, S. Effect of process parameters on electromagnetic impact welding of aluminum sheets. *Int. J. Impact Eng.* **2007**, *34*, 1327–1341. [CrossRef]
- Kumar, S.; Chakravarthy, D.P. Characterisation of electromagnetic welding equipment. *Int. J. Appl. Electromagn. Mech.* **2012**, *40*, 293–300. [CrossRef]

17. Hahn, M.; Weddeling, C.; Lueg-Althoff, J.; Tekkaya, A.E. Analytical approach for magnetic pulse welding of sheet connections. *J. Mater. Process. Technol.* **2016**, *230*, 131–142. [[CrossRef](#)]
18. Watanabe, M.; Kawamura, Y.; Kumai, S. Microstructure and Joint Strength of Magnetic Pulse Welded Aluminum/Aluminum-Coated Steel Joint. *Mater. Trans.* **2021**, *62*, 1151–1159. [[CrossRef](#)]
19. Sarvari, M.; Abdollah-Zadeh, A.; Naffakh-Moosavy, H.; Rahimi, A.; Parsaeyan, H. Investigation of Collision Surfaces and Weld Interface in Magnetic Pulse Welding of Dissimilar Al/Cu Sheets. *J. Manuf. Process.* **2019**, *45*, 356–367. [[CrossRef](#)]
20. Lee, K.-J.; Kumai, S.; Arai, T.; Aizawa, T. Interfacial microstructure and strength of steel/aluminum alloy lap joint fabricated by magnetic pressure seam welding. *Mater. Sci. Eng. A* **2007**, *471*, 95–101. [[CrossRef](#)]
21. Zhou, Y.; Li, C.; Wang, X.; Liao, Z.; Shi, X.; Yao, C. Investigation of flyer plate dynamic behavior in electromagnetic pulse welding. *J. Manuf. Process.* **2021**, *68*, 189–197. [[CrossRef](#)]
22. Li, C.; Zhou, Y.; Shi, X.; Liao, Z.; Du, J.; Shen, T.; Yao, C. Magnetic field edge-effect affecting joint macro-morphology in sheet electromagnetic pulse welding. *Mater. Manuf. Process.* **2020**, *35*, 1040–1050. [[CrossRef](#)]
23. Shim, J.-Y.; Kang, B.-Y.; Kim, I.-S. Characteristics of 5052 aluminum alloy sheets joint using electromagnetic force. *J. Mech. Sci. Technol.* **2017**, *31*, 3437–3444. [[CrossRef](#)]
24. Zhang, H.; Yang, Z.; Ren, L. Experimental investigation on structure parameters of E-shaped coil in magnetic pulse welding. *Mater. Manuf. Process.* **2019**, *34*, 1701–1709. [[CrossRef](#)]
25. Aizawa, T.; Kashani, M. Experimental and numerical study on magnetic pulse welding to improving the life time of one-turn flat coil. *IOP Conf. Ser. Mater. Sci. Eng.* **2014**, *61*, 012028. [[CrossRef](#)]
26. Khalil, C.; Marya, S.; Racineux, G. Construction of physical welding windows for magnetic pulse welding of 5754 aluminum with DC04 steel. *Int. J. Mater. Form.* **2021**, *14*, 843–854. [[CrossRef](#)]
27. Khalil, C.; Marya, S.; Racineux, G. Magnetic Pulse Welding and Spot Welding with Improved Coil Efficiency—Application for Dissimilar Welding of Automotive Metal Alloys. *J. Manuf. Mater. Process.* **2020**, *4*, 69. [[CrossRef](#)]
28. Chari, M.V.K.; Salon, S.J. *Numerical Method in Electromagnetic*; Academic Press: San Diego, CA, USA, 2000; pp. 1–60.
29. Sadiku, M.N.O.; Kulkarni, S.V. *Principle of Electromagnetics*, 6th ed.; Oxford University Press: New Delhi, India, 2015; pp. 383–480.
30. Plonsey, R.; Collin, R.E. *Principles and Applications of Electromagnetic Fields*; McGraw-Hill Book Co.: New York, NY, USA; Toronto, ON, USA; London, UK, 1961.
31. Shotri, R.; Faes, K.; Racineux, G.; De, A. Analytical Estimation of Electromagnetic Pressure, Flyer Impact Velocity, and Welded Joint Length in Magnetic Pulse Welding. *Metals* **2022**, *12*, 276. [[CrossRef](#)]
32. Shotri, R.; Racineux, G.; De, A. Probing magnetic pulse welding of aluminium and steel sheets. *J. Manuf. Process.* **2021**, *72*, 309–319. [[CrossRef](#)]
33. Johnson, G.R.; Cook, W.H. A constitutive model and data for metals subjected to large strains, high strain rates and high temperature. In Proceedings of the Seventh International Symposium on Ballistics, The Hague, The Netherlands, 19–21 April 1983; pp. 541–548.
34. Shotri, R.; Faes, K.; De, A. Magnetic pulse welding of copper to steel tubes—Experimental investigation and process modelling. *J. Manuf. Process.* **2020**, *58*, 249–258. [[CrossRef](#)]
35. Shotri, R.; Racineux, G.; De, A. Magnetic pulse welding of metallic tubes—Experimental investigation and numerical modelling. *Sci. Technol. Weld. Join.* **2020**, *25*, 273–281. [[CrossRef](#)]
36. Faes, K.; Shotri, R.; De, A. Probing magnetic pulse welding of thin-walled tubes. *J. Manuf. Mater. Process.* **2020**, *4*, 118. [[CrossRef](#)]
37. Rebensdorf, A.; Böhm, S. Magnetic pulse welding—Investigation on the welding of high-strength aluminum alloys and steels as well as the influence of fluctuations in the production on the welding results for thin metal sheets. *Weld. World* **2018**, *62*, 855–868. [[CrossRef](#)]
38. ANSYS. *Mechanical Workbench Operations Guide*; Release 14.5; ANSYS Inc.: Canonsburg, PA, USA, 2014.